Journal of Science: Advanced Materials and Devices 9 (2024) 100676

Contents lists available at ScienceDirect

Journal of Science: Advanced Materials and Devices

journal homepage: www.elsevier.com/locate/jsamd

Can ZrAlN thin films be used as thermistor sensors for temperature assessment?

Bruno Martins [a,b,*], Carlos Patacas [a,b], Albano Cavaleiro [a,b], Pedro Faia [c], Oleksandr Bondarchuk [e], Filipe Fernandes [b,d]

[a] IPN - LED&MAT - Instituto Pedro Nunes, Laboratório de Ensaios, Desgaste e Materiais, Rua Pedro Nunes, 3030-199, Coimbra, Portugal
[b] University of Coimbra, CEMMPRE, ARISE, Department of Mechanical Engineering, Rua Luís Reis Santos, 3030-788, Coimbra, Portugal
[c] University of Coimbra, CEMMPRE – Electrical and Computer Engineering Department, FCTUC, Polo 2, Pinhal de Marrocos, Coimbra, 3030-290, Portugal
[d] ISEP - Polytechnic of Porto, Rua Dr. António Bernardino de Almeida, 4249-015, Porto, Portugal
[e] International Iberian Nanotechnology Laboratory (INL), Avenida Mestre Jose Veiga, 4715-330, Braga, Portugal

ARTICLE INFO

Keywords:
NTC thin-film thermistor
Reactive sputtering
Nitride semiconductors
Impedance spectroscopy
Temperature sensing

ABSTRACT

The electrical characteristics and conduction mechanisms of ZrAlN thin films for their potential use as thermistor sensors were assessed. Various compositions of $Zr_{1-x}Al_xN$ were synthesized by sputtering and studied up to 200 °C to understand their sensitivity and applicability. Among the compositions studied, the ones with $x = 0.34$ and $x = 0.46$ showed the highest sensitivities, reaching values close to 3000 K. However, the thermo-resistive properties exhibited by these compositions limited their utilization above 100 °C. $Zr_{1-x}Al_xN$ film compositions with x higher than 0.46 showed amorphous structures and were found to be insulative. Composition with $x = 0.26$, within the cubic phase, showed the most promising electrical properties regarding temperature sensing in the studied range. XPS analysis of this composition confirmed the presence of Zr-N and Al-N bonds, with a Zr^{3+} oxidation state, which suggests the availability of a free electron contributing to the electrical conduction. Impedance measurements performed at different temperatures for this composition revealed the dominant role of the grain boundaries in the conduction mechanism, based upon electron hopping between grains, overcoming the energy barrier imposed by the grain boundaries. ZrAlN thin films demonstrate negative temperature coefficient (NTC) thermistor behavior, expanding their applications beyond protective coatings to temperature monitoring.

1. Introduction

Ternary transition metal nitrides (TMNs) have gathered significant attention in recent decades due to their exceptional properties, such as high hardness, Young's modulus, high-temperature oxidation resistance, and thermal stability. Fine-tuning the thermomechanical properties of stable binary TMNs like ZrN, TiN, and CrN is possible by substituting the transition metal element with aluminum [1–3]. For example, adding Al to ZrN results in significant material property changes [1,4–6]. As the Al content increases, the formation of the Phase-Centered-Cubic, FCC, $Zr_{1-x}Al_xN$ B1 NaCl type phase is favored, which exhibits an increasing trend in hardness, Young's modulus, and oxidation resistance. Beyond the solubility limit of Al in ZrN at $x \approx 0.45$, the nitride outperforms in terms of oxidation resistance but experiences a reduction in hardness and Young's modulus [1,4–6]. Within the miscibility gap, two phases may coexist: defect-rich NaCl-cubic and wurtzite phase mixture, leading to an age-hardening effect upon thermal annealing [7,8]. The single wurtzite phase is achieved at high Al content [6]; however, in most studies, compounds with high Al content tend to form amorphous structures [1,9,10]. Al-rich ZrAlN has been noted for exhibiting Interesting optical and electrical properties [9–11].

Alloying ZrN with Al has been shown to impact its electrical properties, mainly resistivity. The substitution of Zr^{3+} by Al^{3+} in the cubic lattice results in a reduction of the charge carriers and an increase in the resistivity. The effect is further enhanced by the progressive increase of the Al content, which contracts the unit cell, promoting the amorphization of the structure and electron scattering. Additionally, the formation of the hexagonal phase for high Al content increases the

---

Peer review under responsibility of Vietnam National University, Hanoi.

[*] Corresponding author. IPN - LED&MAT - Instituto Pedro Nunes, Laboratório de Ensaios, Desgaste e Materiais, Rua Pedro Nunes, 3030-199, Coimbra, Portugal.
E-mail address: brunomartins@ipn.pt (B. Martins).

https://doi.org/10.1016/j.jsamd.2024.100676
Received 20 November 2023; Received in revised form 17 January 2024; Accepted 21 January 2024
Available online 23 January 2024

Table 1
Deposition parameters used to develop the films.

	Combinatorial ZrAlN	AlN
Ultimate Vacuum (Pa)	$<5 \times 10^{-4}$	$<5 \times 10^{-4}$
Substrates in-situ cleaning – physical etching		
Substrate bias (V)	−650	−650
Time (min)	30	30
Ar pressure (Pa)	0.1	0.1
Targets power density (W.cm^{-2})	0.15	0.15
Pulse frequency (kHz)	245	245
Reverse time (μs)	1.8	1.8
Deposition procedure		
	ZrAlN	AlN
Working pressure (Pa)	≈0.21	≈0.25
Rotation speed (RPM)	–	10
Al Power density (W.cm^{-2})	≈3	≈6 (× 2)
Zr Power density (W.cm^{-2})	≈3	–
Substrate bias (V)	−50	−60
Bias pulse frequency (kHz)	250	250
Bias reverse time (μs)	0.5	0.5
Deposition time (min)	60	60
Target-substrate distance (mm)	–	150
Substrate temperature (°C)	≈160	≈200

resistivity once the hexagonal structure exhibits higher electrical resistivity than the cubic phase [5,9–12]. Significant progress has been made in understanding the electrical behavior of ZrAlN; however, a better comprehension of its resistivity changes with temperature is necessary to explore its potential for temperature-sensing applications. The utilization of ternary TMNs as NTC thermistor sensors has been attained for TiAlN in different studies [13–16]. Replacing Ti with Zr for the same purpose is a plausible solution since they belong to the same group of transition metals with the exact same most common oxidation state of 4^{+}. As Zr^{4+} ions are slightly larger than Ti^{4+} ions, it may change the lattice parameter of the films, resulting in changes in their electrical properties.

As a wear-resistant system, the ZrAlN is well-established in the literature [4–6]. Additional research is necessary to better understand the relationship between the Zr/Al ratio, crystal structure, and semiconductor properties. Moreover, the role of the microstructure, including grain and grain boundaries, in the electrical response remains unclear. To address these questions, ZrAlN thin films were deposited using a combinatorial deposition setup in static mode with varying Zr/Al ratios. Initially, the film's crystal structure was evaluated, and thermo-resistive properties were analyzed. Subsequently, the composition displaying NTC properties within the cubic phase was studied regarding the chemical bond and electrical impedance response. This study offers valuable insights into the conduction mechanisms of the ZrAlN film, known for its wear resistance, and its potential utility as a temperature sensor.

2. Materials and methods

To achieve a chemical gradient by varying the x content in a $Zr_{1-x}Al_xN$ ternary compound, a sputtering system equipped with four magnetrons (380× 175 mm) arranged in a magnetic closed-field configuration and operating in direct current (DC) mode was employed. The schematic containing the substrate holder and Al/Zr targets position is depicted elsewhere [16]. The combinatorial deposition was performed in static mode. An AlN film was deposited using the same equipment, but in rotation mode and used for crystal structure, chemical bonding, and electrical properties comparison. The combinatorial ZrAlN and AlN depositions were carried out in reactive mode, where a gas mixture of N_2 and Ar was introduced into the chamber. A PID (proportional–integral–derivative) mass flow controller regulated the flux based on the working pressure readings obtained with a capacitance pressure sensor.

Before the deposition process, Si (111) substrates were thoroughly cleaned. They were successively immersed in ultrasonic baths filled with acetone, alcohol, and distilled water, each treatment lasting for 10 min. Subsequently, the substrates were air-dried and securely fixed to the substrate holder using silver paste. The holder, along with the substrates, was securely attached to the supports within the vacuum chamber. The chamber was then evacuated until it reached a pressure of 5×10^{-4} Pa. Further information regarding the deposition parameters can be seen in Table 1.

The film's thickness was determined through the ball crater method using a CSEM Calotest® apparatus, with confirmation via a cross-sectional examination conducted with a ZEISS Merlin® field-emission scanning electron microscope (FE-SEM). The crater measurements were executed near the sample's edges to avoid interference with subsequent electrical characterizations. An energy-dispersive X-ray (EDX) technique (Oxford Instrument) was employed in conjunction with a SEM to analyze chemical composition. The crystal structure was assessed using X-ray diffraction (XRD) with Co Kα radiation ($\lambda = 0.178897$ nm) in a Panalytical X'pert equipment in the conventional Bragg-Brentano geometry. Baseline correction was applied to each XRD spectrum, and peak parameters, including the peak position (2θ) and full width at half maximum (FWHM), were calculated by fitting the peaks using a Pseudo-Voigt function. Peak identification was performed using Joint Committee on Powder Diffraction Standards (JCPDS) cards, specifically ZrN 74-1217 and AlN 87-1054, for reference. The lattice constant was determined through Bragg's law equations based on the interplanar distance (d_{hkl}) spacing.

The electrical properties were assessed from room temperature up to 200 °C using the four-point measurement (4PM) technique and electrical impedance spectroscopy (EIS). Four-point measurements were executed using an Ossila four-point probe system, which offers sheet resistance measurements within the range of 100 mΩ.sq^{-1} to 10 MΩ.sq^{-1}, featuring a probe pitch of 1.23 mm. EIS measurements were performed employing a precision impedance analyzer (Agilent 4294A) equipped with built-in Kramers–Kronig relations, featuring excitation frequencies spanning from 10 kHz to 36 MHz and a peak voltage of 500 mV. Separate heating benches were dedicated to the EIS and 4PM procedures. The Agilent system was linked to a cartridge resistor heater, while the Ossila system was connected to a high-speed SiC heater; both were PID-controlled. The 4PM method facilitated resistivity computation based on measured sheet resistance and film thickness at room temperature by applying the equation $\rho = Rs \times t$, where ρ represents resistivity in μΩcm, Rs is sheet resistance in μΩ.sq^{-1}, and t denotes coating thickness in μm. The Ossila Sheet Resistance V2.0.7.1 software was used to apply correction factors automatically, accounting for sample geometric parameters [17].

X-ray photoelectron spectroscopy (XPS) was employed to assess the oxidation states of elements within the films. The analysis was conducted using an ESCALAB 250Xi instrument from Thermo Fisher Scientific, which featured a hemispherical analyzer and a monochromated Al Kα X-ray source operating at 220 W, with a spot size of 650 μm. The XPS spectra were collected with pass energies of 100 eV for survey spectra, used to identify individual elements, and 40 eV for high-resolution spectra. The energy step for high-resolution analysis was set at 0.1 eV. All XPS peaks were calibrated with reference to adventitious carbon C 1s, anchored by a C-C peak at 284.8 eV. Peak fitting was executed by applying a Shirley-type background subtraction method within Origin® software. Notably, the samples did not undergo sputter cleaning before analysis, a deliberate choice to prevent any structural or electrical alterations resulting from ion bombardment.

For all the different chemical compositions investigated in this study, calculations were performed to determine the sensitivity index β, activation energy E_a, and the temperature coefficient of resistance (TCR). The β value was established using the following equation (1):

Table 2
Composition analysis of films using EDX technique. Light elements contaminants are excluded (carbon and oxygen).

	Al/(Al+Zr)								
	0.18	0.26	0.34	0.46	0.59	0.67	0.74	0.83	1
Zr (at%)	39.8 ± 0.4	34.7 ± 0.4	31.0 ± 0.4	25.7 ± 0.4	19.8 ± 0.4	16.2 ± 0.4	12.9 ± 0.4	8.4 ± 0.4	–
Al (at%)	8.4 ± 0.1	12.3 ± 0.1	16.1 ± 0.2	22.1 ± 0.2	28.2 ± 0.2	33.2 ± 0.3	37.1 ± 0.3	42.1 ± 0.4	51.5 ± 0.2
N (at%)	51.8 ± 0.4	53.0 ± 0.4	52.9 ± 0.4	52.2 ± 0.4	52.0 ± 0.4	50.6 ± 0.4	50.0 ± 0.4	49.5 ± 0.4	48.5 ± 0.3

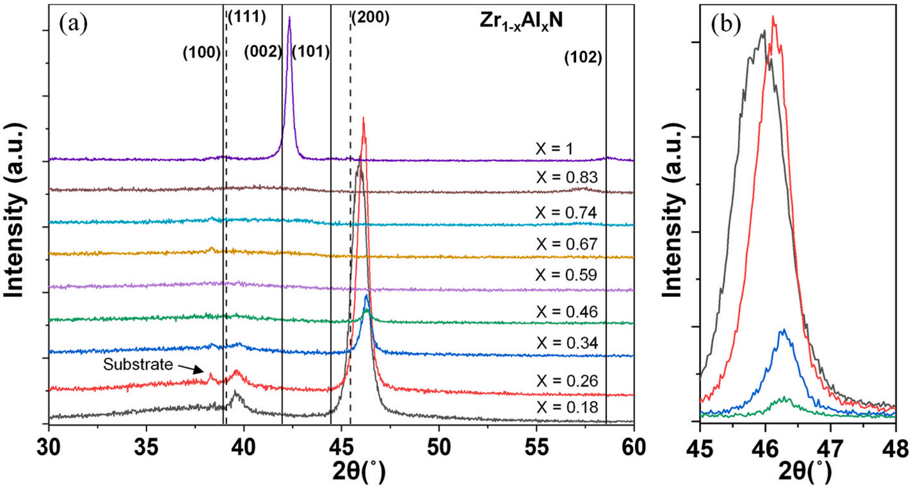

Fig. 1. X-ray diffractogram patterns of $Zr_{1\text{-}x}Al_xN$ films as a function of the Al content and respective standard positions of h-AlN (100)(002)(101)(102), c-ZrN (111) (200) (a). The AlN XRD pattern is referenced as x = 1. The reference card numbers ICDD are ZrN – 87-0633 and AlN 87-1054. Peak shifting detail for $Zr_{1\text{-}x}Al_xN$ coatings where x = 0.18, 0.26, 0.34, 0.46 (b).

$$\beta_{[25-100C]} = \frac{\ln\left(\frac{R_{T1}}{R_{T2}}\right)}{\left(\frac{1}{T_1} - \frac{1}{T_2}\right)} \tag{1}$$

Equation (1) specifies that β is measured in K units, with R_{T1} and R_{T2} representing sheet resistances at temperatures T1 and T2, respectively. The calculation of the temperature coefficient of resistance (TCR) was performed over the identical temperature range as the sensitivity index, and it was determined using equation (2):

$$\mathrm{TCR} = \frac{R_{T2} - R_{T1}}{R_{T1}(T_2 - T_1)} \tag{2}$$

In this other equation, TCR is in units of K^{-1}.

Furthermore, the activation energy was established through an examination of the Arrhenius plot. This method entailed calculating the slope by analyzing the linear relationship between ln(Rs) and 1000/T, where T represents the absolute temperature measured in Kelvin. Subsequently, the activation energy, denoted as E_a and expressed in electron volts (eV), was computed using the formula $E_a = 1000 \times \text{slope} \times k$, where k denotes the Boltzmann constant measured in eV/K.

It is important to highlight that the EIS and XPS assessments were solely conducted on the most favorable film, chosen based on criteria such as crystal structure, chemical composition range, and sensitivity index β. An AlN sample served as a reference throughout the research.

3. Results and discussion

3.1. Chemical composition and structure

The chemical composition of the films is presented in Table 2. As anticipated, the proximity of the substrates to the Al target enabled chemical compositions of higher Al concentrations in the films using the deposition setup depicted in a previous work [16]. The films exhibit a range of Al concentrations, with a minimum recorded value of 7.9 at.% and a maximum of 38.5 at.%. To facilitate the identification of the coatings, they will be referred to as $Zr_{1\text{-}x}Al_xN$, where x represents the Al/(Al+Zr) ratio in the films. All the films displayed a fairly stoichiometric composition since the ratio between metallic elements and N is approximately 1.

Fig. 1(a) shows the XRD diffractograms of the ZrAlN (x varying from 0.18 to 0.83) and AlN films (x = 1). Pure AlN film displays a highly c-axis-oriented hexagonal crystal structure, with a peak shift to higher angles when compared with the (002) ICDD AlN standard position. This shift in peak position can be attributed to the accumulation of stresses during the coating growing process, which was already observed by Liu et al. [18]. Up to x = 0.26, the ZrAlN films display a sharp peak, indicating a (200) preferred orientation of the FCC crystal structure. However, the peak gradually shifts to higher angles considering the ICDD ZrN cubic phase standard position due to the substitution of Zr by Al in the cubic structure. This shift is observed from x = 0.18 to x = 0.46, resulting in changes in the lattice parameters of the crystal structure, which decrease from 4.589 down to 4.554 Å. The peak gradually loses intensity and disappears entirely for x = 0.59, indicating a decrease in the c-ZrN domain. The (111) phase is also observed in the XRD pattern, with a low-intensity peak shifted to higher angles. This diffraction peak disappears for x = 0.46 and beyond. The peak shifting suggests that the incorporation of Al, substituting Zr in the crystal lattice, shrinks the unit cell due to the smaller size of Al. The contraction of the unit cell is communally observed in ternary nitrides, which reflects the reduction in the interatomic spacing within the crystal lattice [2,9–11,16]. Fig. 1(b) shows a detailed view of peak shifting for the XRD diffractogram for the ratios x = 0.18, 0.26, 0.34, 0.46.

Above x = 0.46, the diffraction patterns exhibit an amorphous structure, indicating that the introduction of Al exceeds the solubility limit of the c-ZrN crystal lattice, indicating that the introduction of Al in the c-ZrN lattice destabilizes the structure, impeding the ordered arrangement of the atoms at long distance. This amorphization is

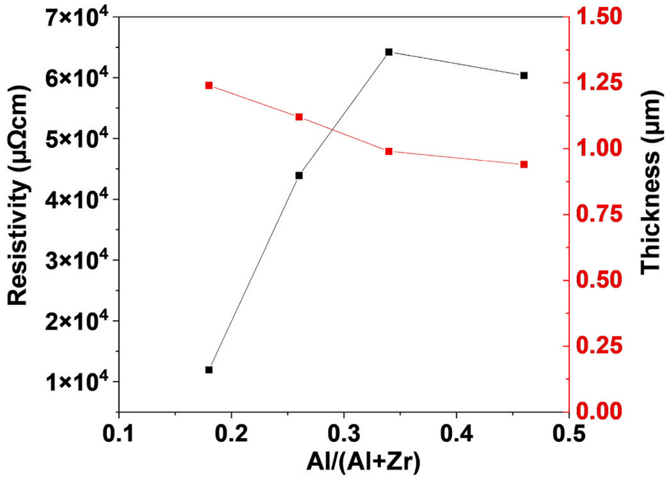

Fig. 2. Resistivity variation according to the Al content in $Zr_{1\text{-}x}Al_xN$ and thickness.

accompanied by the loss of the preferred orientation peak, resulting in a decrease in crystallinity or its complete disappearance. The only exception is the poorly crystalized peak (102) of the AlN hexagonal phase, which is detected for $x = 0.83$. The structural amorphization observed in this work is consistent with previous findings by Meng et al. [10], where the substitution of Zr by Al in the cubic unit cell induced a lattice distortion and the formation of defects, leading to an amorphous phase. The small peak at roughly 37° is referent to the Si substrate.

3.2. Electrical properties

Fig. 2 illustrates the evolution of the sample's resistivity and thickness as a function of the x ratio. As the samples are positioned further away from the targets during deposition, the thickness of the films decreases accordingly. This observation was expected, as the deposition distance affects the film growth rate. Regarding the resistivity, initially, it exhibits a linear increase with Al content increment in the host, demonstrating a clear correlation. This trend continues until $x = 0.34$, where the resistivity achieves its maximum value. However, from $x = 0.34$ up to 0.46, a break from the established trend is observed, leading to a modest decrease in resistivity. It is important to mention that for compositions above $x = 0.46$, the sheet resistance values could not be determined due to the insulation properties of the samples.

The resistivity trend observed for increasing Al content up to $x = 0.36$ is in concordance with what was expected for the ZrAlN compound [9,10,12]. The substitution of Zr by Al reduces the number of free electrons, decreasing available charge carriers within the material [5,10]. Additionally, the presence of the insulating AlN phase increases in opposition to the decreasing conductive ZrN phase. These combined effects contribute to the anticipated increase in resistivity with rising Al content. However, for $x = 0.46$, the resistivity trend deviates from the predictable behavior. As the Al content increases, a disordered state is induced within the crystal structure, further increasing resistivity [10]. The disordered arrangement of atoms and the presence of defects (vacancies or dislocations) hinder the flow of charge carriers. On the other hand, the lack of long-range order may lead to unexpected variations in the electrical properties, which is believed to occur for the poorly crystallized sample with $x = 0.46$. In the study conducted by Liu et al. [19], the authors provide valuable insights into the relationship between resistivity fluctuations and amorphous structures. They specifically investigated amorphous molybdenum silicide thin films and found that particular surface disorder could lead to discrepancies in the resistivity measurements.

The resistivity achieved during the present study for films with the lowest Al content is approximately one order of magnitude higher than those developed by Lamni et al. [9] and Meng et al. [10]. The discrepancy in resistivity, compared to the reported values by these authors, suggests the influence of structural factors. The XRD spectrum confirms the amorphization of the structure with increasing Al content, a characteristic also observed by Araiza et al. [20] in their study on ZrN.

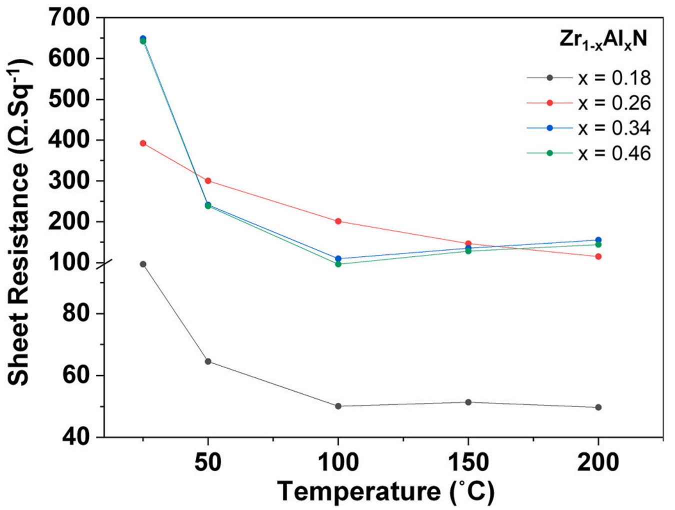

Fig. 3. Sheet resistance measurement across various chemical compositions at temperatures ranging from room temperature to 200 °C in ambient air. The lines are provided as visual guides for the reader.

Table 3
Analysis of sensitivity, activation energy, and TCR across different chemical compositions. Sensitivity and TCR were computed in the temperature range [25-100 °C], while activation energy was derived from the linear relationship between lnRs and 1000/T depicted in Fig. A1 of the supplementary material.

Al/(Al+Zr)	β [K]	E_a [meV]	TCR [K^{-1}]
0.18	966.8	80.3	-6.4×10^{-3}
0.26	990.5	85.0	-6.5×10^{-3}
0.34	2639.7	442.3	-1.1×10^{-2}
0.46	2816.0	444.4	-1.1×10^{-2}

The sheet resistance of $Zr_{1\text{-}x}Al_xN$ compositions was investigated as a function of temperature up to 200 °C, and the results are presented in Fig. 3. Across all measured compositions, a consistent semiconductor behavior characterized by a negative TCR is observed. However, a trend reversal is identified for samples with $x = 0.34$ and 0.46, occurring above 100 °C, where the resistance-temperature curve exhibits a slightly positive slope. This phenomenon can be ascribed to the well-known thermo-resistive effect commonly encountered in semiconductors [21]. As the temperature rises, the number of charge carriers in the conduction band increases, resulting in a decrease in resistivity. This behavior is evident in the 25–100 °C temperature range for all compositions investigated in this study. For samples with $x = 0.34$ and 0.46, a distinct response emerges above 100–200 °C. In this range, the concentration of free charge carriers originated in the extrinsic region reaches a saturation point, accompanied by a subsequent decrease in mobility due to the temperature effect. Consequently, this decrease in mobility contributes to a slightly positive temperature coefficient (PTC). Such a region is frequently referred to as the saturation region and holds significance in developing semiconductors that maintain their conductivity independently of the temperature. This saturation region was already reported by Martins et al. [16] in their study on TiAlN, where specific compositions exhibit similar trends. It is worth mentioning that the investigation of this specific region is beyond the scope of the current study.

Table 3 summarizes the sensitivity, TCR, and activation energy results obtained for the $Zr_{1\text{-}x}Al_xN$ thin films compositions depicted in

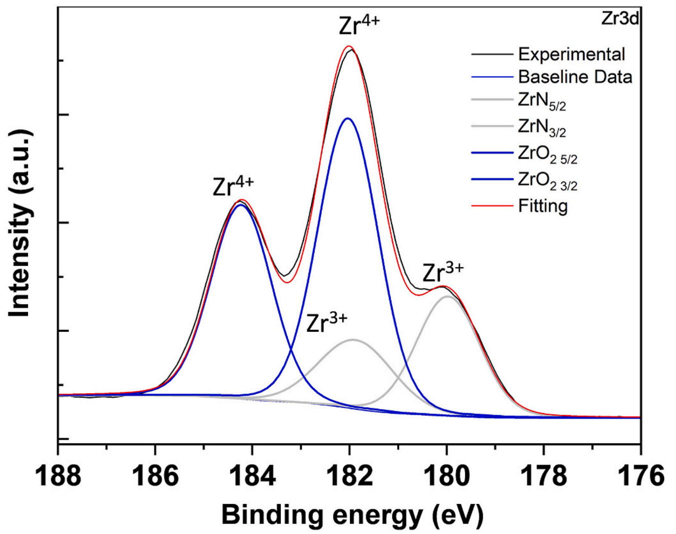

Fig. 4. HR XPS spectra for Zr 3d of sample $Zr_{1-x}Al_xN$ for x = 0.26. Shirley's background was used for peak fitting.

Figs. 2 and 3. The data demonstrates that the sensitivity, activation energy, and TCR exhibit a consistent increase with increasing x ratio. The observed trends confirm that the composition has a direct influence on the electrical properties, emphasizing the Al content's role in shaping the film's electrical behavior. Moreover, the increase in the activation energy implies a decrease in the carrier density in the conduction band, which means that fewer charge carriers are available for conduction, suggesting a more insulating nature.

A significant change occurs for compositions of $x > 0.26$, for which both the sensitivity and the activation energy exhibit a three-fold increase when compared to compositions with lower x values. In addition, the TCR shows a one-order-of-magnitude rise for the highest x ratios. A possible explanation for this increment is the loss of crystallinity in the (200) phase, which is evident for compositions with x = 0.34 and 0.46. Interestingly, the electrical behavior for the samples with x = 0.34 and 0.46 are comparable, suggesting a similar response to temperature changes within this specific range of compositions. However, for the sample with x = 0.46, the sensitivity does not follow the same trend as resistivity, i.e., it increases while resistivity remains unchanged. These changes can be attributed to the amorphization of the film, as discussed earlier, which can lead to slightly scattered results.

Finally, the values found in Table 3 highlight the possibility of tuning the electrical properties through chemical composition manipulation. The ability to control the Al content allows for tailoring the sensitivity, TCR, and activation energy, optimizing $Zr_{1-x}Al_xN$ films for specific applications. The highest achieved sensitivity values closely approach those reported in the literature for Mn-based metal oxides [22–24]. Furthermore, the sensitivity values surpass those reported for cubic TiAlN films [13,16], demonstrating their better performance in terms of electrical response.

3.3. *Chemical states*

The selection of a specific composition for further investigation using X-ray photon-electron spectroscopy was taken by carefully considering their electrical characteristics. Among the investigated compositions, the ones with x = 0.34 and 0.46 exhibit the highest sensitivities, indicating their potential usage as thermistor sensors. However, their behavior above 100 °C makes them less suitable for high-temperature environments commonly encountered in wear applications. For example, the cutting temperatures achieved during cutting tests of the aluminum 6061 alloy (usually low-temperature alloys) were around 130 °C [25]. Hence, the composition with x = 0.26 exhibits the most promising electrical properties compared to the one with x = 0.18. In fact, it exhibits the highest sensitivity within the highly crystalline cubic phase of the metastable compound, making it a suitable candidate for temperature sensors. Based on the observations, authors carried on and performed XPS analysis on the film with x = 0.26 and the pure AlN for comparison purposes. Fig. 4 displays the high resolution - HR XPS spectra for Zr in $Zr_{1-x}Al_xN$, while Fig. 5 (a to d) compares obtained HR

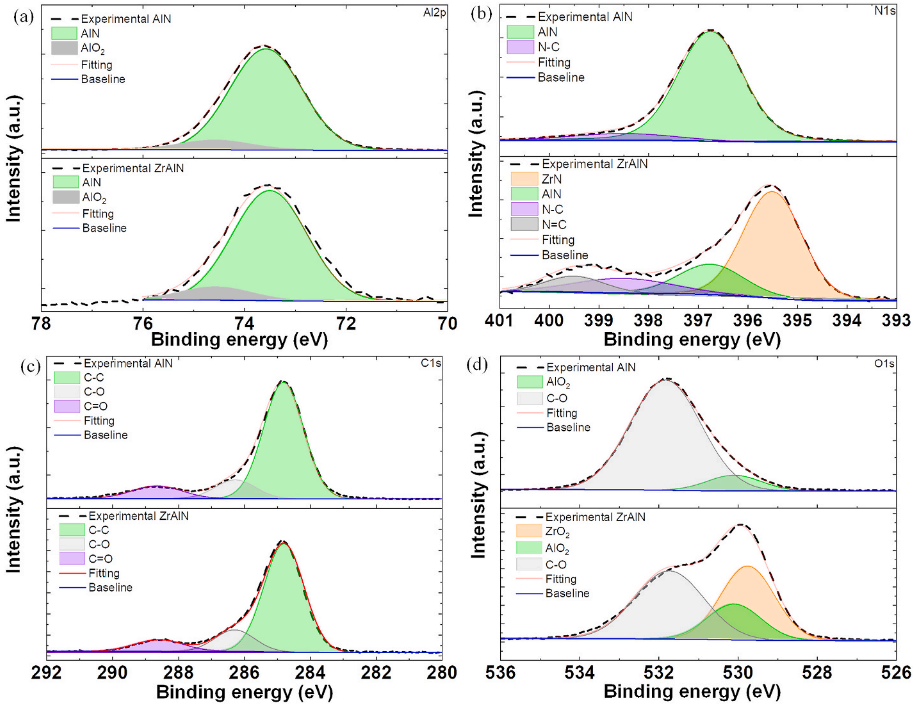

Fig. 5. XPS spectra comparing elemental composition of $Zr_{1-x}Al_xN$ for x = 0.26 and AlN. High-Resolution (HR) Spectra are presented for Al 2p (a), N 1s (b), C 1s (c), and O 1s (d). Peak fitting performed using Shirley's background.

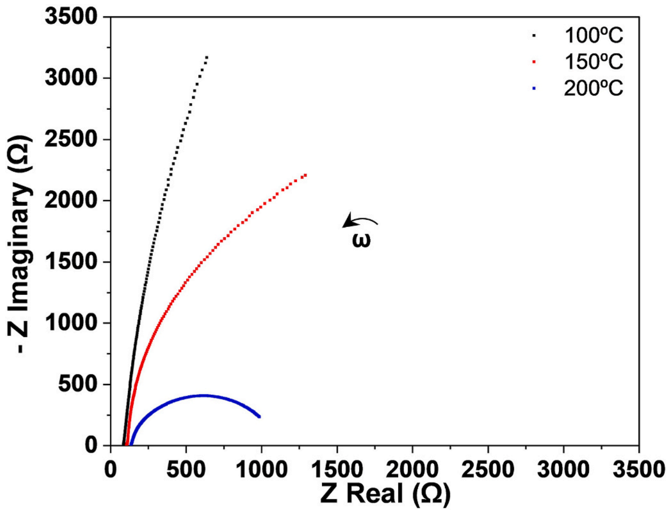

Fig. 6. Nyquist plots depiction for sample $Zr_{1-x}A_xlN$, for x = 0.26. Assigned temperatures 100 °C (black line), 150 °C (red line), and 200 °C (blue line).

XPS spectra ZrAlN and AlN for Al, N, O, and C elements.

In the Zr 3d spectra, the spin-orbit splitting doublets Zr $3d_{5/2}$ and Zr $3d_{3/2}$ are observed, exhibiting a typical spacing of approximately 2 eV, consistent with previously published studies [7,26,27]. The deconvolution of the spectra revealed two distinct peaks at 180 and 182.1 eV, which are assigned to Zr^{3+} and Zr^{4+} oxidation states, respectively [7,26–28]. The assigned Zr oxidation state peaks align well with the expected compounds, particularly ZrN and ZrO_2, indicating the presence of these elements in the material. However, the presence of oxide peaks can be attributed to surface native oxidation, likely resulting from exposure to air.

Analyzing the N 1s spectra, three prominent peaks are observed for the AlN sample. Considering the Al 2p spectra, the prominent peak observed at 73.6 eV corresponds to AlN, which is consistent with previous reports [26,29]. Additionally, the small peak detected at higher binding energies can be attributed to the Al-O bond derived from surface native oxidation. The peaks at 395.5 and 396.8 eV can be ascribed to metal nitrides, corresponding to ZrN and AlN, respectively, according to the literature [26,29]. The peak at 398.4 eV is likely associated with impurities or organics [29]. An extra peak appears in the N 1s spectra for ZrAlN at 399.4 eV, which can be attributed to adsorbed nitrogen [27,30].

Regarding the O 1s spectrum, three peaks are discernible at 529.8, 530.1, and 531.8 eV, which can be assigned to metal oxides and C-O bonds from adventitious contamination [29]. The metal oxide bonding is likely attributed to Al^{3+} and Zr^{4+} species [29,30]. The C 1s spectra exhibit three peaks at 284.8, 286.2, and 288.6 eV. The first peak corresponds to C-C surface contamination and serves as a reference for peak position correction [26,30]. The small peaks observed at 286.2 and 288.6 eV can be attributed to C-O and C=O bonds commonly associated with organic contaminants [30].

The presence of N-Ti and N-Al bonds is evident upon analyzing the XPS spectra, indicating the formation of nitride compounds within the material. It is important to note that the presence of carbon and oxygen bonds is expected since the samples were not subjected to physical etching or cleaning procedures prior to XPS acquisition, allowing the retention of surface contaminants. Additionally, surface oxidation is observed due to exposure of the sample to air. As a result, the Zr^{4+} oxidation state shows no substantial impact on the conduction mechanism, whereas the presence of a Zr^{3+} peak from the Zr-N bond suggests that Zr possesses a free electron from the dxy orbital. This free electron is available for conduction, contributing to the electrical properties of the material. These observations agree with the previously observed trend of the activation energy increasing with a decrease in Zr content, indicating a reduction in the number of free electrons at the donor level.

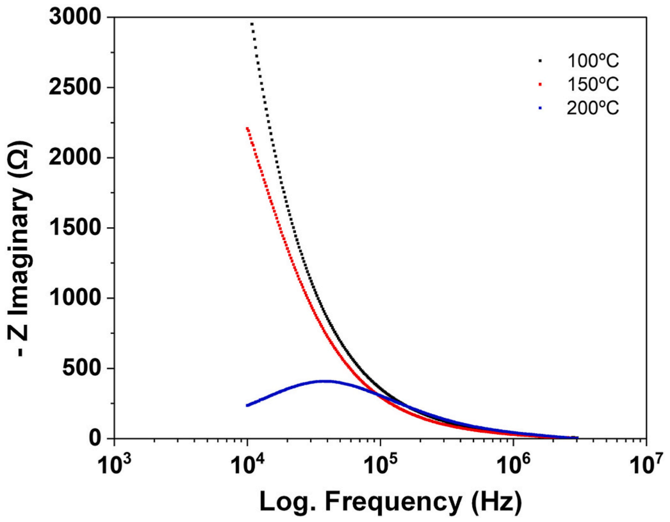

Fig. 7. Variation of the imaginary part with frequency across different temperatures for $Zr_{1-x}A_xlN$, x = 0.26. Assigned temperatures 100 °C (black line), 150 °C (red line), 200 °C (blue line).

3.4. Electrical impedance spectroscopy

The AC impedance analysis was conducted on the sample that underwent XPS analysis, allowing for a comprehensive understanding of its electrical response. Two silver epoxy glue electrodes were used to measure the impedance at 100 °C, 150 °C, and 200 °C. Nyquist plots are commonly used to represent complex impedance spectra, providing valuable insights into the contributions of grain boundaries, grains, and electrode polarization across low to mid and high frequencies, respectively [31]. In Fig. 6, the Nyquist diagram illustrates the complex impedance spectra plot for the ZrAlN sample at temperatures 100, 150, and 200 °C. From the spectra analysis, an arc of an uncomplete semi-circle, with a large radius, is observed at 100 °C. As the temperature increases, the arc gradually closes, and at 200 °C, the semi-circle becomes more evident without intersecting the real axis at low frequencies. This behavior suggests that the contribution of the grain boundaries to the conduction mechanism is higher than that of the grain [24]. The interception with the real axis at the high-frequency limit is relatively similar for all three temperatures, reflecting the resistance of the electrodes and the wiring components. The Nyquist plot for the AlN is not represented since it exhibits a straight line overlapping the real axis, lacking any reactive component. This behavior confirms, and is in accordance with, its electrical insulating nature.

The behavior of the imaginary part of the impedance in response to frequency, plotted in Fig. 7, provides insights into the dominant role of the grain boundaries in the overall conduction mechanism. At 100 °C and 150 °C, the imaginary part of the impedance exhibits an exponential decrease with increasing frequency, highlighting the significant impact of the reactive component at low frequencies. This behavior indicates that, at those temperatures, the contribution of the grain boundaries surpasses that of the grain itself, emphasizing their role in the conduction. In contrast, at 200 °C, the presence of a bell-shaped curve suggests the occurrence of a relaxation phenomenon at a characteristic frequency. Once the characteristic frequency is positioned away from low frequencies, it signifies an increasing influence of the grain effect on the conduction mechanism, attributed to the bulk effect and typically associated with the conduction band [31]. As a result, electron hopping plays a dominant role in the conduction mechanism of the sample, which occurs between grains, effectively surpassing the energy barriers

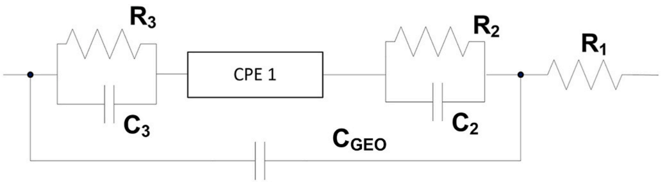

Fig. 8. Representation of the model for the equivalent circuit.

imposed by the grain boundaries [32]. This observation is consistent with the available electron from Zr, as revealed by XPS analysis, suggesting its role in facilitating the hopping process. In addition, it can be concluded that the sample reveals NTC behavior since the total impedance decreases with temperature.

The impedance spectra can be effectively represented by an equivalent circuit composed of a set of elements, allowing for the modeling of the various phenomena associated with the observed conduction and polarization processes. It is important to note that impedance spectra portray a range of electrical and polarization phenomena; therefore, multiple equivalent circuit models can provide satisfactory fits to the experimental data. The selection of the most appropriate circuit should consider simplicity and alignment with established physical and chemical principles for our samples [33]. Consequently, based on the spectra analysis, an equivalent circuit model was developed, depicted in Fig. 8, to describe the observed behavior.

The initial parameters of the model were determined using EIS spectra analyzer software and subsequently fine-tuned manually. The proposed model incorporates the following contributions: 1) R_1, representing the resistance of the electrodes and wiring components; 2) CPE1, a constant phase element representing the conduction contribution along interface inhomogeneities between the electrodes and the material, and along the sample surface. The CPE impedance is defined as $1/(Q(j\omega))^n$, where Q is the admittance when $\omega = 1$ rad/s, and $0 < n < 1$, and can exhibit capacitive or resistive behavior depending on the value of the exponent n [34]; 3) $R_2//C_2$ and $R_3//C_3$, which comprise resistor-capacitor pairs, stand for the contributions of grain boundaries and bulk granular, respectively; 4) C_{GEO}, a geometric capacitance accounting for the electrode configuration resembling parallel plates, with the material under test in-between. Fig. 9 presents examples of the fittings, showcasing the alignment between the proposed model and the experimental data in both the Nyquist and Bode representations.

Table 4 contains the key electrical response characteristics for the ZrAlN sample with $x = 0.26$ at different temperatures. As the temperature exceeds 150 °C, the components of the constant phase element (CPE), denoted as Q and n, indicate an increase in the capacitive part of the impedance. This suggests a minor separation of the silver electrodes from the sample surface. Similarly, the resistance associated with the electrodes and wiring components, represented by R1, also rises with increasing temperature. The combined resistance, consisting of R2 and R3, decreases with temperature, consistent with the typical negative temperature coefficient (NTC) behavior observed in the materials under investigation. Moreover, the significance of the charge transfer mechanism in detrimental of the double layer interface is emphasized, as the contribution of capacitive elements C2 and C3 remains limited.

The time constants ($\tau = C \times R$) for grain and grain boundaries – associated with the frequencies for which each region responds –

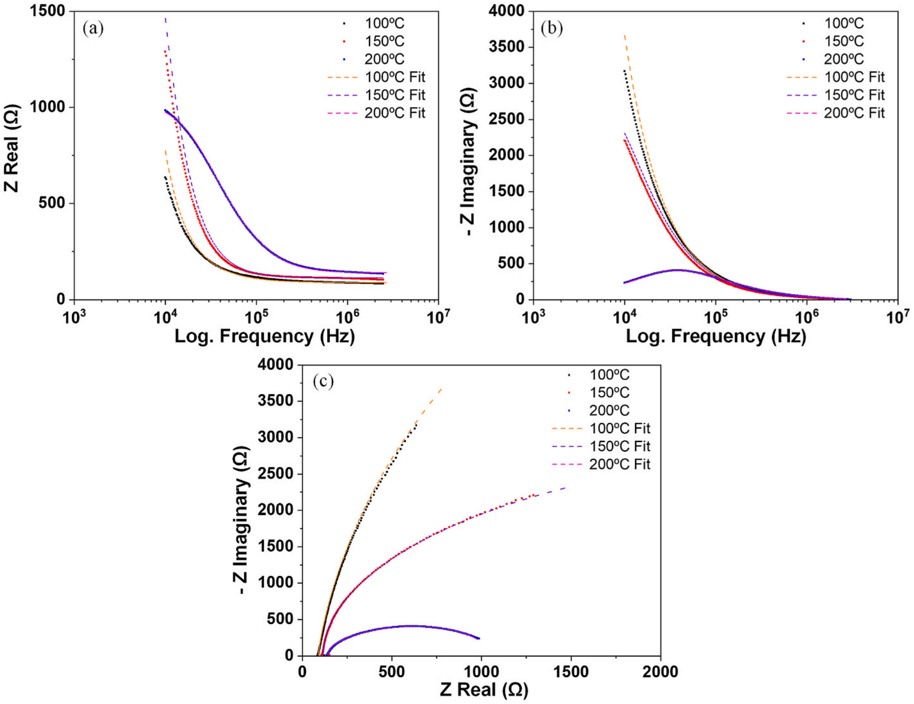

Fig. 9. Fitting demonstrations employing the equivalent circuit model for $Zr_{1-x}Al_xN$, with $x = 0.26$, at the investigated temperatures: 100, 150, and 200 °C (Graphs (a), (b), and (c) – Real-Frequency; Imaginary-Frequency; Nyquist).

Table 4
Fitted parameters for the equivalent circuit model for $Zr_{1-x}Al_xN$ with $x = 0.26$.

Temperature (°C)	R_1 (Ω)	R_2 (Ω)	C_2 (F)	R_3 (Ω)	C_3 (F)	C_{GEO} (F)	Q (Ω^{-1})	n (a.u)
100	89.3	8227.6	1.8×10^{-9}	728.7	4.1×10^{-11}	4.9×10^{-9}	5.68×10^{-7}	0.48
150	113.3	4447.7	6.9×10^{-9}	392.5	3.2×10^{-8}	4.5×10^{-10}	1.5×10^{-7}	0.94
200	140.4	697.9	7.0×10^{-9}	196.8	7.3×10^{-9}	5.8×10^{-11}	1.15×10^{-6}	0.98

support the fact that grains contribution regarding conduction displays increasing importance as the temperature increases. For instance, at 100 °C, the calculated time constant for the grain boundary is 1.5×10^{-5} s, while for the grain region is of 3.0×10^{-8} s, showing the slower reaction time of the grain boundaries. As the temperature increases to 200 °C, the values change to 4.9×10^{-6} and 1.4×10^{-6} s, respectively. The shorter difference between time constants at 200 °C suggests that the charge distribution dynamics happen almost simultaneously; however, it is still slightly longer for the grain boundary. The latter statement is supported by the fact that while the contribution of the grain to the overall conduction mechanism increases with temperature, the grain boundary effect remains relatively higher. Observing the fitted components for the equivalent circuit proposed in Yang et at. study [35] it is possible to reveal nearby time constants for the grain and grain boundaries contributions. Therefore, electron hopping is the dominant conduction mechanism in ZrAlN up to 200 °C, predominantly occurring along the grain boundaries.

4. Conclusion

This work aimed to explore the electrical characteristics and conduction mechanisms of ZrAlN thin films to assess their potential usage as temperature sensors, specifically thermistors. Various compositions of $Zr_{1\text{-}x}Al_xN$ were studied, among which the one with $x = 0.34$ and 0.46 exhibited the best sensitivities, with values approaching 3000 K. Nevertheless, the compositions revealed thermos-resistive effect and, as a consequence, their application as thermistor sensors is limited to low-temperature environments, by showing both extrinsic and metal-like regions. $Zr_{1\text{-}x}Al_xN$ composition with $x = 0.26$, within the cubic phase, was the one that showed the most promising electrical properties, making it a suitable candidate to be employed as a temperature sensor.

The XPS analysis of the composition with $x = 0.26$ revealed the existence of nitrides by detecting Zr-N and Al-N bonds. The prevalence of the Zr^{3+} oxidation state in the bonds suggests the involvement of a free electron from the Zr dxy orbital in the conduction mechanism. For the same composition, the impedance measurements indicate that grain boundaries significantly impact conduction mechanisms up to 200 °C. Therefore, it is assumed that the Zr loosely bounded electron promotes hopping between grains by surpassing the energy barrier imposed by the grain boundaries. In addition, the convergence between time constants of grain and grain boundaries with increasing temperature indicates that intrinsic conduction is established beyond 200 °C.

In summary, the present work demonstrated that it is possible to develop ZrAlN thin film thermistors with different compositions and structures using the sputtering technique. Although the β value obtained for the cubic composition is lower than oxide thermistors, it has the potential for high-temperature measurements.

CRediT authorship contribution statement

Bruno Martins: Investigation, Writing - Original Draft, Visualization. Carlos Patacas: Investigation, Visualization. Albano Cavaleiro: Writing - Review & Editing, Supervision, Validation, Conceptualization. Pedro Faia: Investigation, Writing - Review & Editing. Oleksandr Bondarchuk: Investigation. Filipe Fernandes: Writing - Review & Editing, Supervision, Validation, Conceptualization.

Declaration of competing interest

The authors declare that they have no known competing financial interests or personal relationships that could have appeared to influence the work reported in this paper.

Acknowledgements

This research is sponsored by national funds: Soft4Sense project "Smart Surfaces for Reliable Tooling Integration" (reference: POCI-01-0247-FEDER-045921), co-financed by the European Regional Development Fund, through Portugal 2020 (PT2020), by the Competitiveness and Internationalization Operational Programme (COMPETE 2020) and Foundation for Science and Technology (FCT) is also acknowledged. This research is also sponsored by national funds through FCT, under projects UIDB/00285/2020 and LA/P/0112/2020.

Appendix A. Supplementary data

Supplementary data to this article can be found online at https://doi.org/10.1016/j.jsamd.2024.100676.

References

[1] N. Ghafoor, I. Petrov, D. Holec, G. Greczynski, J. Palisaitis, P.O.A. Persson, L. Hultman, J. Birch, Self-structuring in Zr1−xAlxN films as a function of composition and growth temperature, Sci. Reports - Nat. 8 (2018) 1–17, https://doi.org/10.1038/s41598-018-34279-w.

[2] M. Danek, F. Fernandes, A. Cavaleiro, T. Polcar, Influence of Cr additions on the structure and oxidation resistance of multilayered TiAlCrN films, Surf. Coating. Technol. 313 (2017) 158–167, https://doi.org/10.1016/j.surfcoat.2017.01.053.

[3] A. Liu, J. Deng, H. Cui, Y. Chen, J. Zhao, Friction and wear properties of TiN, TiAlN, AlTiN and CrAlN PVD nitride coatings, Int. J. Refract. Met. Hard Mater. 31 (2012) 82–88, https://doi.org/10.1016/j.ijrmhm.2011.09.010.

[4] R. Franz, M. Lechthaler, C. Polzer, C. Mitterer, Oxidation behaviour and tribological properties of arc-evaporated ZrAlN hard coatings, Surf. Coating. Technol. 206 (2012) 2337–2345, https://doi.org/10.1016/j.surfcoat.2011.10.023.

[5] R. Lamni, R. Sanjinés, M. Parlinska-Wojtan, A. Karimi, F. Lévy, Microstructure and nanohardness properties of Zr–Al–N and Zr–Cr–N thin films, J. Vac. Sci. Technol. A Vacuum, Surfaces, Film. 23 (2005) 593–598, https://doi.org/10.1116/1.1924579.

[6] X.Y. Zhu, J. Du, G.M. Liu, X.H. Zheng, Influence of al-content on the microstructure and mechanical properties in ZrALN coatings, Adv. Mater. Res. 1004–1005 (2014) 778–783. https://doi.org/10.4028/www.scientific.net/AMR.1004-1005.778.

[7] L. Rogström, L.J.S. Johnson, M.P. Johansson, M. Ahlgren, L. Hultman, M. Odén, Age hardening in arc-evaporated ZrAlN thin films, Scripta Mater. 62 (2010) 739–741, https://doi.org/10.1016/j.scriptamat.2010.01.049.

[8] L. Rogström, L.J.S. Johnson, M.P. Johansson, M. Ahlgren, L. Hultman, M. Odén, Thermal stability and mechanical properties of arc evaporated ZrN/ZrAlN multilayers, Thin Solid Films 519 (2010) 694–699, https://doi.org/10.1016/j.tsf.2010.08.119.

[9] R. Lamni, R. Sanjinés, F. Lévy, Electrical and optical properties of Zr1-xAlxN thin films, Thin Solid Films 478 (2005) 170–175, https://doi.org/10.1016/j.tsf.2004.10.049.

[10] J. ping Meng, K. Zhang, X. peng Liu, Z. qiang Fu, Z. Li, Influence of the aluminum content on structure and optical properties of Zr1-xAlxN films, Vacuum 145 (2017) 268–271, https://doi.org/10.1016/j.vacuum.2017.08.045.

[11] G. Ke, Y. Tao, Z. He, H. Guo, Y. Chen, J. Dibattista, E. Chan, Y. Yang, Influence of sputtering atmosphere on crystal quality and electrical properties of zirconium aluminum nitride thin film, Surf. Coat. Technol. (2015), https://doi.org/10.1016/j.surfcoat.2015.09.046.

[12] M. Magnuson, W. Olovsson, N. Ghafoor, M. Odén, L. Hultman, Interface bonding of Z r1-x A lx N nanocomposites investigated by X-ray spectroscopies and first principles calculations, Phys. Rev. Res. 2 (2020) 1–12, https://doi.org/10.1103/PhysRevResearch.2.013328.

[13] T. Fujita, H. Tanaka, H. Inaba, N. Nagatomo, Development and electrical properties of wurtzite (Al,Ti)N materials for thin film thermistors, J. Ceram. Soc. Japan. 124 (2016) 653–658, https://doi.org/10.2109/jcersj2.15316.

[14] M. Yoshikawa, D. Toyama, T. Fujita, N. Nagatomo, T. Makimoto, Hole conduction characteristics of cubic Ti1−xAlxN, Thin Solid Films 660 (2018) 711–714, https://doi.org/10.1016/j.tsf.2018.04.010.

[15] S. Suzuki, T. Fujita, Y. Hosokawa, K. Fujiwara, N. Nagatomo, Development of a wurtzite (Al,Ti)N thermistor on a resin substrate with high heat resistance, J. Ceram. Soc. Japan. 129 (2021) 355–358, https://doi.org/10.2109/jcersj2.20224.

[16] B. Martins, C. Patacas, A. Cavaleiro, P. Faia, O. Bondarchuk, F. Fernandes, Electrical properties and thermistor behavior of TiAlN thin films deposited by combinatorial sputtering, Surf. Coat. Technol. 464 (2023) 129545, https://doi.org/10.1016/j.surfcoat.2023.129545.

[17] I. Miccoli, F. Edler, H. Pfnür, C. Tegenkamp, The 100th anniversary of the four-point probe technique: the role of probe geometries in isotropic and anisotropic systems, J. Phys. Condens. Matter 27 (2015) 223201, https://doi.org/10.1088/0953-8984/27/22/223201.

[18] H.Y. Liu, G.S. Tang, F. Zeng, F. Pan, Influence of sputtering parameters on structures and residual stress of AlN films deposited by DC reactive magnetron sputtering at room temperature, J. Cryst. Growth 363 (2013) 80–85, https://doi.org/10.1016/j.jcrysgro.2012.10.008.

[19] Z. Liu, B. Luo, Disorder-induced transport peculiarities in amorphous molybdenum silicide thin films, Phys. Status Solidi Basic Res. 257 (2020), https://doi.org/10.1002/pssb.202000165.

[20] J.J. Araiza, O. Sánchez, J.M. Albella, Influence of the aluminum incorporation on the structure of sputtered ZrNx films deposited at low temperatures, Vacuum 83 (2009) 1236–1239, https://doi.org/10.1016/j.vacuum.2009.03.012.

[21] T. Dinh, H.P. Phan, A. Qamar, P. Woodfield, N.T. Nguyen, D.V. Dao, Thermoresistive effect for advanced thermal sensors: fundamentals, design considerations, and applications, J. Microelectromech. Syst. 26 (2017) 966–986, https://doi.org/10.1109/JMEMS.2017.2710354.

[22] W. Kong, J. Wang, J. Yao, A. Chang, Influence of oxygen atmosphere annealing on the thermal stability of Mn1.2Co1.5Ni0.3O4±δ ceramic films fabricated by RF magnetron sputtering, Ceram. Int. 44 (2018) 1455–1460, https://doi.org/10.1016/j.ceramint.2017.10.040.

[23] T. Xuan, J. Yan, J. Wang, W. Kong, A. Chang, Characterization of Al-doped Mn–Co–Ni–O NTC thermistor films prepared by the magnetron co-sputtering approach, J. Alloys Compd. 831 (2020) 154831, https://doi.org/10.1016/j.jallcom.2020.154831.

[24] Ruifeng, Q. Fu, X. Zou, Z. Zheng, W. Luo, L. Yan, Mn-Co-Ni-O thin films prepared by sputtering with alloy target, J. Adv. Ceram. 9 (2020) 64–71, https://doi.org/10.1007/s40145-019-0348-y.

[25] D. Werschmoeller, X. Li, Measurement of tool internal temperatures in the toolchip contact region by embedded micro thin film thermocouples, J. Manuf. Process. 13 (2011) 147–152, https://doi.org/10.1016/j.jmapro.2011.05.001.

[26] I. Bertóti, Characterization of nitride coatings by XPS, Surf. Coating. Technol. 151–152 (2002) 194–203, https://doi.org/10.1016/S0257-8972(01)01619-X.

[27] G. Zhan, J. Liu, J. Guo, J. Feng, B. Xu, B. Yang, X. Chen, C. Yang, Electrical transport property of zirconium oxynitride thin film deposited by magnetron sputtering process, J. Mater. Sci. Mater. Electron. 26 (2015) 9188–9194, https://doi.org/10.1007/s10854-015-3610-2.

[28] J.F. Moulder, Handbook of X-Ray Photoelectron Spectroscopy: A Reference Book of Standard Spectra for Identification and Interpretation of XPS Data, Physical Electronics Division, Perkin-Elmer Corporation, 1992.

[29] C. Badini, S. Deambrosis, E. Padovano, M. Fabrizio, O. Ostrovskaya, E. Miorin, G. D'Amico, F. Montagner, S. Biamino, V. Zin, Thermal shock and oxidation behavior of HiPIMS TiAlN coatings grown on Ti-48Al-2Cr-2Nb intermetallic alloy, Materials 9 (2016) 961, https://doi.org/10.3390/ma9120961.

[30] M. Matsuoka, S. Isotani, W. Sucasaire, N. Kuratani, K. Ogata, X-ray photoelectron spectroscopy analysis of zirconium nitride-like films prepared on Si(100) substrates by ion beam assisted deposition, Surf. Coating. Technol. 202 (2008) 3129–3135, https://doi.org/10.1016/j.surfcoat.2007.11.019.

[31] X. Sun, H. Zhang, Y. Liu, J. Guo, Z. Li, Characterization of new negative temperature coefficient thermistors based on Zn–Ni–O system, J. Adv. Ceram. 5 (2016) 329–336, https://doi.org/10.1007/s40145-016-0206-0.

[32] G. Zhan, Z. Lin, B. Xu, J. Feng, B. Yang, X. Chen, C. Yang, J. Liu, Study of temperature sensitivity and impedance spectroscopy of zirconium oxynitride thin film thermistors, J. Mater. Sci. Mater. Electron. 28 (2017) 9653–9657, https://doi.org/10.1007/s10854-017-6715-y.

[33] J.E. Bauerle, Study of solid electrolyte polarization by a complex admittance method, J. Phys. Chem. Solid. 30 (1969) 2657–2670, https://doi.org/10.1016/0022-3697(69)90039-0.

[34] K. Fujiwara, S. Lee, N. Donnelly, T. Yamaguchi, C.A. Randall, Resistance degradation in Y(Cr,Mn)O3-Y2O3 composite NTC ceramics in hostile environments, J. Am. Ceram. Soc. 92 (2009) 2634–2641, https://doi.org/10.1111/j.1551-2916.2009.03253.x.

[35] B. Yang, H. Zhang, J. Zhang, X. Zhang, Z. Li, Electrical properties and temperature sensitivity of B-substituted CuO-based ceramics for negative temperature coefficient thermistors, J. Mater. Sci. Mater. Electron. 26 (2015) 10151–10158, https://doi.org/10.1007/s10854-015-3701-0.